Cell

## EXTENDED EXPERIMENTAL PROCEDURES

### Transient Expression in Protoplasts and Coimmunoprecipitation

Transformation of *Arabidopsis* protoplasts was performed essentially as described (Fülöp et al., 2005) by transfecting 5 × $10^5$ cells with 3 μg each of myc-CDK and HA-CYCD expression constructs. Transfected cells were cultured for 16 hr at RT, then harvested by centrifugation and lysed in extraction buffer containing 25 mM Tris-HCl pH 7.8, 10 mM $MgCl_2$, 5 mM EGTA, 75 mM NaCl, 60 mM beta-glycerophosphate, 2 mM DTT, 0.2% Igepal CA 630, 0.1 mM $Na_3VO_4$, 1 mM benzamidine and protease inhibitors (Protease Inhibitor Coctail for plant cells, Sigma).

Equal amounts of proteins were subjected to coimmunoprecipitations in a total volume of 100 μl extraction buffer supplemented with 150 mM NaCl, 0.2 mg $ml^{-1}$ BSA and 1.5 μg of antibody against HA (HA.11 clone 16B12, Covance) or c-Myc epitopes (c-Myc clone 9E10, Covance). Immunocomplexes were captured on 10 μl of Protein G-Sepharose beads (GE Healthcare), washed three times in TBS buffer containing 5% glycerol and 0.1% Igepal CA 630, then eluted by boiling with 30 μl Laemmli sample buffer and subjected to SDS-PAGE. Following gel separation proteins were blotted onto Immobilon-P PVDF transfer membrane (Millipore), and stained with Ponceau S. For immunodetection of tagged proteins monoclonal anti-HA-peroxidase conjugate (clone 3F10, Roche), monoclonal anti-c-Myc (clone 9E10, Covance) and chicken anti-c-Myc (Molecular Probes) antibodies and the SuperSignal West Pico Chemiluminescent Substrate (Thermo Scientific) were used.

### SCR-RBR Interaction In Planta

Col-0 and 35S::SCR-GFP seeds were germinated on 0.5x MSAR, 1% sucrose plates under long day conditions and roots of seven days old seedlings were collected. Samples were first grinded in liquid nitrogen then extracted with ice cold extraction buffer and clarified by centrifugation at 14,000 rpm for 15 min at 4°C. Protein concentration was measured by Bradford assay (Biorad) and 150 μg of proteins were incubated with 20 μl GFP-Trap magnetic beads (Chromotek) in a final volume of 200 μl of extraction buffer supplemented with 150 mM NaCl, 0.2 mg $ml^{-1}$ BSA for two hours at 4°C on a rotating wheel. Beads were washed three times with TBS buffer containing 5% glycerol and 0.1% Igepal CA 630 then proteins were eluted by boiling with 30 μl Laemmli sample buffer. Affinity purified fraction was analyzed on protein gel blots with an antibody specific for the *Arabidopsis* RBR protein and monoclonal anti-GFP (clone B34, Covance).

### Plant Growth Conditions

Seeds were sterilized in 5% sodium hypochlorite, imbibed at 4°C in the dark in sterilized water containing 0.1% agarose for 2 days and germinated on plates containing 0.5x Murashige and Skoog (MS) salt mixture, 1% sucrose, and 0.5g/l 2-(N-morpholino) ethanesulfonic acid (MES) at pH 5.8, in 0.8% plant agar. Plates were incubated in a near vertical position at 22°C with a 16h light/8h dark cycle. *Arabidopsis thaliana* Columbia-0 (Col-0) was used as wild-type and as the background in all transgenic and mutant lines (*scr4-1* is WS).

### CEI Division Frequency Analysis

40 and 36 roots of respectively *cdkb1;1 cdkb1;2* mutant or Col-0 WT were used to count the presence of a CEI or CEID. The number of CEI and CEID were divided by the total number of ground tissue cells layers analyzed to obtain the CEI/CEID frequency. Frequencies obtained from plants grown on the same plate were used to calculate the average CEI/CEID frequency and for t test analysis.

### Plant Materials Used for This Study

All plant materials used in this study and relevant references are given in Table S5.

### Expression Constructs and Entry Clones

All expression constructs and entry clones used in this study and relevant references are given in Table S5.

#### *Hydroxyurea-Mediated Synchronization and Fluorescence Intensity Quantitation*

For synchronization seeds from each transgenic line tested were germinated in MS medium and transferred 5 dpg to phytagel-MS medium containing 2 mM HU (adapted from Cools et al., 2010).

To determine protein dynamics prior and during mitosis we measure mean pixel intensity of the whole cell with the same area using Leica LCSlite 2.0 (Leica Microsystems) software. For pSHR::SHR:YFP (n = 75 cells prior and 39 during mitosis), pSCR::SCR:YFP (n = 58 cells prior and 31 during mitosis) and pRBR::RBR:CFP (n = 25 cells prior and 12 during mitosis). For qualitative and quantitative comparison of protein degradation or stabilization, images were recorded with identical confocal settings in all cases. The average intensity prior mitosis was considered as 100% for each transgenic line and compared to the average of the cells during mitosis. Significant differences between measurements were identified with Student's *t test*.

#### *MG132 Treatment*

Five-day-old seedlings grown in MS plates were transferred to liquid MS added with 50 μg/ml MG132 (Sigma and Biomol; dissolved to 50 mg/ml in DMSO) or with 0.1% DMSO alone as control, for 4 hr at 20°C in the light before observation and recording.

### ChIP-Q-PCR Position in NUC Promoter and Used Primers

Positions between primers upstream the starting codon: NUC6:-4935-4786 (−4,9); NUC5:-4503-4390: (−4,4); NUC4:-3995-3896: (−3,8); NUC3b:-2944-2812: (−2,9); NUC3a:-2320-2155, (−2,2); NUC2: −1282-1133, (−1,2). Fragment size ranges between 100 and 165 bp. A list of all primers used is given in Table S5.

## Modeling Procedures

During our study it turned out to be essential to analyze regulatory circuit dynamics within the spatial context of the tissue. Given the multiple, non-linear feedback loops involved, we adopted a mathematical and computational approach to unravel the mechanisms that determine which cells undergo asymmetric stem cell divisions. To study the regulatory circuit, we developed a set of coupled ordinary differential equations (ODEs), which we considered capturing the dynamics of the important interacting components within each cell. Those ODEs were subsequently integrated within the tissue context.

Mathematical analysis of the well-determined interactions that are presented in the main text shows that the feedbacks involved can create different steady states, which fall into two categories: either high levels of SHR-SCR are found, which is considered to trigger the ACDs, or low levels are found, leading to ordinary cell divisions within the cell files. Note that the modeling effort presented in this paper does not attempt to explain what causes the cell division to be asymmetric nor the repositioning of the cell plate during the CEI/CEID cell divisions, hence, the models do not explicitly describe the ACDs themselves. Rather, the modeling deals with how the cellular positioning of the ACD is determined and coordinated within a tissue, by flipping, at the correct positions and influenced by the root tissue layout, to the ACD-related cell state. We have studied three different models which, by analyzing them consecutively, have helped to reveal key issues and features of ACD determination.

### Model 1 or "Double Positive Feedback Model": Linking Cellular Switch-like Behavior to Tissue Radial Patterning

The first model presents the *minimal requirements* to produce a switch-like ACD behavior, capable of transforming the SHR gradient along the radial axis into a well-defined radial boundary. We begin by presenting model 1 and the related analyses. We will then treat the limitations presented by this model which have instigated the development of further extensions as well as further experiments, which will be discussed further below.

A severe limitation for quantitative mathematical modeling of this regulatory network is the fact that detailed measurements regarding protein and complex concentrations and production and degradation rates are only marginally available. Moreover, for all processes described within the network, the dissociation constants are basically unknown, so our quantitative knowledge is limited to the overarching timescales of the observed dynamics and abundances of the proteins. We therefore opted to formulate all equations in the basic form of mass action kinetics, except when mass action kinetics would lead to unrestrained growth of mathematical terms. The first model is based on two important experimental observations: the complex formation between SCR and RBR (Figure S1) and the observation that SCR is required to keep SHR nuclearly localized. In accordance to our experimental data, we assume that SCR unbound to RBR and nuclear SHR are required in conjunction for activating: (i) the ACDs, in the sense that the state in which both unbound SCR and nuclear SHR are high is the ACD-related cell state; (ii) enhanced SCR production; and (iii) CYCD6;1 production.

*The ODE Model.* The ODE model is given by:

$$\text{cytosolic SHR}: \quad \frac{dH_c}{dt} = p_{H_c} - c_{H_n} H_c S + c_{H_c} H_n z - d_{H_c} H_c \tag{1a}$$

$$\text{nuclear SHR}: \quad \frac{dH_n}{dt} = \frac{c_{H_n} H_c S}{z} - c_{H_c} H_n - d_{H_n} H_n \tag{1b}$$

$$\text{SCR}: \quad \frac{dS}{dt} = p_{S1}\left(\frac{H_n S}{1 + (H_n + S)/c_S}\right) + p_{S2} - c_T S(r - R - T) - d_S S \tag{1c}$$

$$\text{CYCD6; 1}: \quad \frac{dC}{dt} = p_C\left(\frac{H_n S}{1 + (H_n + S)/c_S}\right) - d_C C \tag{1d}$$

$$\text{RBR}^{\text{P}}: \quad \frac{dR}{dt} = c_R C(r - R - T) - d_R R \tag{1e}$$

$$\text{SCR-RBR}: \quad \frac{dT}{dt} = c_T S(r - R - T) - d_T T \tag{1f}$$

The above model describes protein or complex concentrations within a single cell. Experimentally we can clearly discriminate between SHR located in the cytosol and SHR located in the nucleus (see, e.g., Figures 6G and 6H). Importantly, SHR can only diffuse between cells through plasmodesmata when located in the cytosol, and only activate downstream targets when located in the

nucleus. We therefore distinguish between cytosolic SHR ($H_c$) and nuclear SHR ($H_n$). Cytosolic SHR has a basic production rate ($p_{H_c}$) and can enter the nucleus, which depends on SCR, $S$ ($c_{H_n}SH_c$), whereas nuclear SHR can leave the nucleus to become localized again inside the cytosol ($c_{H_c}H_n$). Similar results were found when SCR instead stabilizes SHR in the nucleus, reducing its exit rate (data not shown). Note however that such dynamics cannot be captured using a single mass-action term. To describe the concentration increase due to SHR entering the nucleus we have to take into account the relatively small volume of the nucleus compared to the cytosol. Hence a correction factor $z$ is brought in, representing the percentage of the cell occupied by the nucleus ($(c_{H_n}H_cS)/z$). Likewise, SHR moving back into the cytosol again requires the correction factor $z$ to capture the consequential increase in cytosolic SHR concentration ($c_{H_c}H_nz$). Finally, cytosolic SHR has a basic turnover/decay term ($d_{H_c}H_c$), and a similar turnover/decay term is used for all variables in our model (i.e., $d_{H_n}H_n$, $d_SS$, $d_CC$, $d_RR$, and $d_TT$). Regarding the turnover, please note that we explicitly assume degradation, but no dissociation of the SCR-RBR complex. The results do not change when dissociation is also considered, provided its rate is relatively low. SCR which is not bound to RBR is described by the variable $S$. In accordance with published observations, there is a small background production of SCR, $S$ ($p_{S2}$), but its production can be geared up by the combined action of SCR and nuclear SHR ($(p_{S1}H_nS)/(1+(H_n+S)/c_S)$). Note that we explicitly require both nuclear SHR and SCR for SCR activation, nuclear SHR alone not being sufficient. We use here a saturation term to keep the levels of $H_n$ and $S$ bounded. Without such a saturation and using only mass-action terms, their levels would become, for many parameter settings, infinitely large. The saturation, however, does not play a role in the generation of bistability. Note that it is not always realized that the conventional Michaelis-Menten term, derived for the description of enzyme kinetics, makes the hidden assumption that complex formation reduces the effective concentration of only one of the variables, while not affecting the other (i.e. it assumes that one variable is at a much lower concentration than the other, which is typically the enzyme of a reaction with substrate in excess). In many situations, especially non-enzyme contexts, this is clearly an invalid assumption. Borghans et al. (1996) therefore developed an improved Michaelis-Menten term, employed here, based upon the so-called Total Quasi Steady State assumption, which better captures the dynamics when there is no *a priori* reason to assume a large concentration difference. SCR can bind to RBR, to form SCR-RBR, $T$. We here take the simplifying view that the total concentration of RBR per cell remains constant (given by the parameter $r$), but that only the non-phosphorylated form can bind to SCR. The total amount of RBR that is available to bind is given by total RBR minus $RBR^P$, $R$, and RBR within the SCR-RBR complex, $T$. Taking this into account, the total amount of RBR available to bind equals $(r-R-T)$, and the rate by which SCR binds to RBR is therefore given by $c_TS(r-R-T)$. The combined action of SCR and nuclear SHR is able to activate the production of CYCD6;1, $C$. For this activation we use a similar response as used for the SCR activation ($(p_CH_nS)/(1+(H_n+S)/c_S)$). Finally, CYCD6;1, in its turn, causes phosphorylation of non-phosphorylated RBR ($c_RC(r-R-T)$). Note that this equation for $RBR^P$ implicitly assumes that de novo RBR production gives rise to non-phosphorylated RBR only, whereas CYCD6;1 is essentially required for its phosphorylation.

*Spatial Embedding of the ODE Model.* Within the spatial model, each individual cell contains the same regulatory network, whereas the spatial coupling between cells takes place through cytosolic SHR, $H_c$, which is able to diffuse between cells. In the model we use concentrations rather than total protein content of cells, given that concentration differences, and not total protein amount itself, drives the fluxes between the cells. Note that because the cells can have very different sizes, the concentration can be the same, whereas the total protein content can be quite different.

*Root Layout.* As realistic root layouts for our simulations, we have been using both digitized microscopy images of the root and more caricature-like layouts, which capture all essential elements of the root tip. Because, for the questions asked in this specific study, the real and caricature layout do not present different outcomes or insights, we here only show the results for the caricature layout, which allows us to show the results in a clearer fashion. For the simulations we are using a two-dimensional (2D) grid, representing a cross-section through the root, in which the bilateral symmetry of the root across the xylem axis is captured. For the grid we use a spatial resolution of 0.5 μm.

Figures S3A and S3C shows the detailed layout of the root used in the simulations, with all the different cell types indicated. It is partly based on earlier studies, in which we used a rectangular layout (Grieneisen et al., 2007; Laskowski et al., 2008). For the unraveling of the organization within the stem cell niche, however, it turned out to be essential to take the specific structure within the stem cell niche into account.

*SHR Transport.* The level of cytosolic SHR as determined by the regulatory network and intercellular diffusion is captured by a single concentration value for each cell. We here describe the spread of SHR through the cells by means of plasmodesmata as a diffusive process. The diffusion of SHR between cells is therefore calculated in the following way. First, we assumed that the diffusion predominantly takes place through plasmodesmata, and that the cell wall therefore does not have to be taken into account. We then used the total shared boundary length between cells (ignoring the cell wall) and the distance between the centroids of the cells to calculate the effective diffusive flux between them:

$$\overrightarrow{J_H}(i\rightarrow j) = D_H L(i,j)\frac{H_c(i)-H_c(j)}{\left|\vec{i}-\vec{j}\right|},$$

where $\overrightarrow{J_H}(i\rightarrow j)$ is the flux from cell $i$ to cell $j$; $D_H$ is the diffusion rate of SHR; $L(i,j)$ is the shared boundary length between $i$ and $j$; $H_c(i)$, $H_c(j)$ are the cytosolic SHR concentrations in both cells, and $\vec{i}$, $\vec{j}$ vectors to the centroid of both cells. Note that the protein movement is here described as a purely diffusive process, hence dependent on the distance between the cell centers and the length of

shared cell wall between the cells. If alternatively passage through the plasmodesmata would be the only factor limiting SHR spread, it should instead be described as a transport process dependent on the length of shared cell wall between the cells, not on the distance between the cells. In reality, the flux will be limited by a mixture of both cytosolic diffusion and transport through the plasmodesmata. Here, however, we have not explored these details further. The change in concentration is given by:

$$\frac{\partial H_c(i)}{\partial t} = \frac{-\sum_k \overrightarrow{J_H}(i \rightarrow k)}{V(i)},$$

where $V(i)$ is the total area of cell $i$, and $k$ sums over all direct neighbors of the cell. Within the root tip there is quite a large variation in cell size, whereas the size of the nucleus typically only marginally differs between cells. The parameter $z$, which stands for the fraction of the cell occupied by the nucleus, is therefore taken into account as a cell-specific property: $z(i) = V_n/V(i)$, where $V_n$ is the typical nuclear area, and $V(i)$ the total cell area of cell $i$.

In the spatial model we further assume that only vascular and pericycle cells produce SHR (i.e., for all other cell types $p_{H_c} = 0$), and that inversely all but the vascular and pericycle cells have a small background production of SCR (i.e., for vascular and pericycle cells, $p_{S2} = 0$). The parameter values used are shown in Table S2. They were chosen to represent realistic dynamics and timescales. The equations were solved by using the Runge-Kutta 4th order method, with $\Delta t = 10^{-3}$ s.

*Model 1 Presents Switch-like ACD Behavior.* While our final results strongly emphasize the importance of the spatial integration of the system, we here present further analysis on the ODEs that describe the dynamics at the single cell level, as this allows us to better dissect the robustness of the models and to make apparent what arises due to cellular interactions and tissue context. We first asked the question what would be the equilibrium SCR and nuclear SHR levels in the ODE version of model 1 (Equation 1), for different levels of production cq. influx of SHR. We therefore created a bifurcation diagram by varying $p_{H_c}$ and observing the equilibria and their stability. Figure 3H depicts the equilibria in terms of SCR levels unbound to RBR, $S$. It shows that bistability can be found over a very wide range of SHR influx levels. One stable steady state presents very high $H_n$ and $S$ levels, corresponding to the ACD cell state, while the other stable steady state presents low $H_n$ and $S$ levels, corresponding to the default cell behavior. The stable steady states are separated by an unstable saddle point, which presents a threshold that needs to be crossed to switch from one state to the other. For low values of SHR influx there is only one stable state, illustrating that sufficient SHR influx is needed to gain the *potential* of the ACD cell state, while very high SHR influx (more than 25 times higher than the SHR influx into CEI/CEID/endodermal cells at our default parameter settings) causes the low equilibrium to disappear, leading to the *flip* to the ACD cell state.

*Dissecting the Bistability: The Importance of a Double Feedback Loop.* To dissect what feedbacks are required for triggering the ACD behavior, and to analyze their individual contributions as well as their combined actions, it is very helpful to graphically capture the cause of the bistability. For model 1 this is possible by combining the methods of quasi-steady-state (QSS) analysis and nullcline analysis. QSS analysis allows us to reduce the number of independent variables within a system. It is typically done when certain variables are varying on a much faster timescale relative to the others, but it can also be applied for a more general analysis on the number of equilibria within a system. Importantly, a QSS analysis never changes the number of equilibria in a system, and can therefore be straightforwardly applied to determine those. (The stability of those equilibria can change though, in the sense that equilibria that are found to be stable after the QSS reduction of the number of variables could in fact be unstable in the original model.) QSS analysis allows the reduction of model 1 to two independent variables, nuclear SHR, $H_n$, and SCR not bound to RBR, $S$:

$$\text{cytosolic SHR}: \quad H_c = \frac{p_{H_c} + c_{H_c} H_n z}{c_{H_n} S + d_{H_c}} \tag{2a}$$

$$\text{CYCD6;1}: \quad C = \frac{p_C}{d_C}\left(\frac{H_n S}{1 + (H_n + S)/c_S}\right) \tag{2b}$$

$$\text{RBR}^{\text{P}}: \quad R = \frac{r c_R d_T C}{c_R d_T C + d_R c_T S - d_R d_T} \tag{2c}$$

$$\text{SCR-RBR}: \quad T = \frac{r d_R c_T S}{c_R d_T C + d_R c_T S - d_R d_T} \tag{2d}$$

$$\text{nuclear SHR}: \quad \frac{dH_n}{dt} = \frac{c_{H_n} H_c S}{z} - c_{H_c} H_n - d_{H_n} H_n \tag{2e}$$

$$\text{SCR}: \quad \frac{dS}{dt} = \frac{p_{S1} H_n S}{1 + (H_n + S)/c_S} + p_{S2} - c_T S(r - R - T) - d_S S \tag{2f}$$

Having reduced the system to two independent variables enables two-dimensional phase-plane analysis, which eases graphical representation. In Figures 3I and S2E, we show the phase-plane of nuclear SHR, $H_n$, against SCR unbound to RBR, $S$, both on a logarithmic scale, as well as the nullclines and vector field for the above model, Equation 2. The intersections of the nullclines indicate the equilibria of the system. As the lines cross thrice, this indicates three equilibria. Two of them are stable, separated by an unstable equilibrium, a saddle, i.e., it illustrates the bistability.

To dissect to which extent the bistability is either due to the SCR transcription feedback loop (i.e., due to the fact that SCR unbound to RBR in the presence of nuclear SHR is activating SCR transcription) or due to the CYCD6-mediated feedback loop (i.e., due to the fact that SCR unbound to RBR and nuclear SHR activate CYCD6;1, which effectively leads to RBR phosphorylation, and hence more SCR unbound to RBR), we generated nullclines for the cases where one or both of the feedback loops are removed (which can be done by setting $p_{S1}$ and/or $p_c$ to zero). Although the shape of nullclines are modified, the qualitative behavior of bistability is preserved when one of the feedbacks is removed (Figures 3J, 3K, S2F, and S2G). However, if both are turned off, the system fails to present bistability for any possible parameter setting (Figures 3L and S2H). We therefore conclude that it is the combined (and redundant) action of two feedback loops which determines the huge potential for bistability underlying the behavior of ACD specification.

Within the spatial simulations, however, the SHR influx-dependent bistability leads to two possible scenarios. Because SHR production is limited to the vasculature while degraded everywhere, a radial gradient in SHR levels is formed. One possibility is that the highest SHR levels, found close to the vasculature, are not sufficient to flip to the ACD state. In that case SHR keeps its graded radial distribution. Alternatively, the positive feedback loops are sufficiently strong (e.g., because the value of $p_c$ is higher) that the cells close to the vasculature reach SHR levels that are above the fold bifurcation, and hence enter the ACD cell state. In the latter case the nuclearization of SHR in the endodermis due to the high SHR-SCR levels prevents further spread of cytosolic SHR, reducing the SHR levels beyond the endodermis to close to zero. Consequently, the spatial simulations present a very strong radial pattern, in which only a single cell file differentiates, even when the initial SHR gradient could have triggered the ACD cell state in cell files further outward. Importantly, the effect that the activation of the ACD has on the SHR gradient itself causes the sharp, reliable, single-cell-layer-wide response, with strongly deviating expression levels for a whole range of proteins, to an initially more shallow and possibly very variable radial gradient. The importance of the response to a morphogen gradient on the gradient itself has been elucidated before for animal systems (Jaeger et al., 2008).

In short, while the first model cannot explain why ACDs are limited to specific cells rather than the whole endodermal cell file, it has allowed us to link cellular switch-like behavior to robust radial patterning within the tissue. Model 1, or the ''double positive-feedback model'' (1) has the *minimal requirements* to produce the switch-like ACD behavior; (2) shows how the SHR gradient along the radial axis can be transformed in a radial switch; and (3) allows us to understand through nullcline analysis the role of the two positive feedback loops.

### *Model 2 or "Auxin-Regulated Double Positive Feedback Model": Longitudinal Precision of Switch*

After establishing that the experimentally derived model could explain the radial, but not the longitudinal patterning, we explored whether it would be theoretically possible that the auxin gradient discovered previously (Grieneisen et al., 2007) could supply the required longitudinal cue. We required that an auxin-dependent link in the regulatory network should not only confine the ACD cell state to the correct cells, but should also capture all the different dynamics observed in wild-type and mutants and during interferences. We found that when the effect of auxin was brought into the model through an auxin-dependent modification of the *CYCD6;1* activation rate, all these requirements were met, while this was not straightforwardly the case for other choices, such as auxin inhibiting the RBR phosphorylation by *CYCD6;1* or auxin inhibiting the formation of the SCR-RBR complex. This generated a hypothesis of auxin-augmented *CYCD6;1* activation, which was confirmed experimentally. In the second model we therefore introduce auxin into the network (model 2, aka the ''auxin-regulated double positive-feedback model''), through an auxin-dependent activation of *CYCD6;1* by modifying Equation (1d),

$$\text{CYCD6;1: } \frac{dC}{dt} = p_C \left( \frac{X^h}{c_X^h + X^h} \right) \left( \frac{H_n S}{1 + (H_n + S)/c_S} \right) - d_C C, \tag{3}$$

where $X$ represents the average auxin concentration within the cell. The parameter $c_X$ indicates the auxin concentration at which the auxin-mediated *CYCD6;1* activation is half-maximal, and $h$ is the so-called Hill-coefficient, indicating the steepness of the sigmoidal relationship. We have used, in contrast to all other terms, a sigmoidal Hill function, in order to describe a relatively steep dependency of *CYCD6;1* activation on auxin. This steep dependency was derived from the fact that the AxCxA mutant and/or auxin treatment only presents a limited expansion of the zone in which ACDs are observed, but is not required nor relevant for the bistability presented by the model (see section on high robustness below). The steepness of the Hill coefficient, $h = 3$, has been based upon the experimental observations on the SCR AxCxA mutant and the auxin treatments: in simulations with a non-sigmoidal dependency we observed more dramatically expanded ACDs in the $SCR^{AxCxA}$ background and/or when the root was treated with auxin. Please note, however, that instead of a sigmoidal dependency on auxin, these observations could alternatively be caused by other, non-linear saturations within the cell-autonomous network itself (data not shown).

*Spatial Implementation of Auxin Transport.* To model the auxin flow in the spatial model, each cell consists of multiple grid points, such that auxin concentrations may vary within cells. The cell wall is described as a separate entity, one grid point (0.5 μm) wide.

Auxin flow through a cell requires influx permeability, bringing auxin into the cell across the membrane, diffusion within the cell, and efflux permeability, allowing auxin to cross the membrane and enter the cell wall space. Once in the cell wall space, auxin can freely diffuse until it reaches a membrane. In the basic model, influx is given by a constant permeability rate, $P_{in}$, in units of $\mu m/s$. Thus, we do not take for example any differential AUX1 expression levels into account, but assume influx to be homogeneous for all cells and along all their membrane. In contrast, auxin efflux permeability is assigned a strong $(P_{e_{SPIN}})$, weak $(P_{e_{WPIN}})$, or background $(P_{e_{bg}})$ value, depending on the level of PIN export facilitators at the membrane. The choice of level and orientation of the PINs was determined by visual inspection of images showing the location and intensity of fluorescent PIN fusion proteins (see Laskowski et al., 2008). Background efflux permeability $P_{e_{bg}}$ is fixed at 5% of the permeability resulting from high intensity PIN expression. All parameters are shown in Table S2.

Diffusion of auxin takes place within cells and cell walls and is given by $\overrightarrow{J_X} = -D_X \vec{\nabla} X$, where $D$ corresponds to the diffusion rate, given in units of $\mu m^2/s$ (note that in contrast permeability rates carry the unit of $\mu m/s$), and $X$ corresponds to the auxin concentration, given in arbitrary units [a.u.]. In the cell wall, auxin diffusion is slower, modeled by a reduction factor $k$: $\overrightarrow{J_X} = -D_X/k \vec{\nabla} X$. Diffusion is not permitted across cell membranes (i.e., no flux boundary conditions). The flux due to auxin permeability across a membrane can be written as

$$\overrightarrow{J_X} = \begin{cases} -\left(P_{e_{SPIN}} \hat{\mathbf{n}}\right) X_{in} + \left(P_{in} \hat{\mathbf{n}}\right) X_{out} & \text{if PINs are expressed strongly,} \\ -\left(P_{e_{WPIN}} \hat{\mathbf{n}}\right) X_{in} + \left(P_{in} \hat{\mathbf{n}}\right) X_{out} & \text{if PINs are expressed weakly,} \\ -\left(P_{e_{bg}} \hat{\mathbf{n}}\right) X_{in} + \left(P_{in} \hat{\mathbf{n}}\right) X_{out} & \text{if only background efflux takes place,} \end{cases} \quad (4)$$

where $\hat{\mathbf{n}}$ is the inward directed unit vector, perpendicular to the membrane; $X_{in}$ represents the auxin concentration in the cytosol at the grid point bordering the cell membrane; and $X_{out}$ represents the auxin concentration in the cell wall grid point immediately adjacent to the cell membrane. Simulations of auxin dynamics are performed by concurrently solving for the diffusion, permeability and decay of auxin, using an Alternating Direction Implicit (ADI) method (Peaceman and Rachford, 1955). The boundary conditions at the shootward end of the simulated root segment, which guarantee a constant influx of auxin into the root, are implemented exactly as described previously (Laskowski et al., 2008).

*PIN Localization.* An important aspect of the auxin transport model is the intracellular localization of the different PIN proteins, which drive the directed auxin transport through the cells. To be able to localize within the model specific PINs rootward, shootward or laterally, requires defining, for each cell, which part of its membrane is orientated in those different directions. For rectangular cells this is a trivial task, but in the more complex layout this required a different strategy. We have developed an algorithm that compartmentalizes each cell into four different zones, which are, relative to the centroid of the cell, oriented upward, downward, inward, or outward. Figures S3B and S3D shows for each cell those different zonations in green, purple, cyan, and red, respectively. When, for a specific cell type, we want to position PINs along a certain direction, we make use of all membrane positions within that zone (and belonging to cells of the required cell type; Figures S3A and S3C), and position within the model the PIN proteins at those grid points. The orientations used for PIN localization are indicated in Table S1.

*Auxin Confines ACDs to CEI/CEID.* In the spatial simulations of model 2 the ACDs are confined to the CEI/CEID (see Figures 4O and 4P). In the analysis of model 1 we pointed out that both feedback loops act redundantly to generate the required bistability. In contrast, model 2 shows that each feedback loop is essential for the correct spatial patterning, with the SCR-transcription feedback loop required for reaching high SCR levels and making the two possible states very distinct, while the feedback loop through CYCD6;1 is essential for the auxin-mediated augmentation, required for the longitudinal precision of the switch. The next question, however, is the robustness of this bistability-generating network, given the high level of uncertainty in the parameter values, and whether the network, when embedded within the spatial context of the root, is able to preserve the correct spatial pattern, with only the CEI/CEID cells entering the ACD cell state, when parameter values are diverging from the default ones.

*High Robustness of Circuit due to Feedback Loops.* We first checked for the default set of parameter values the range over which bistability can be observed when varying parameters one at a time (see Table S2). This revealed that for all parameters the range over which bistability is yielded is huge. Such a parameter sweep, however, does not answer the question if this robustness stems from the particular choice of our default combination of parameters.

We therefore continued with a more thorough study on the robustness of the regulatory circuit (Equation 1 and Equation 3). Because the equations were formulated and the parameters defined to capture specific biological meanings, they are not necessarily independent from one another. Moreover, when screening for the parameter range for which specifically the bistable behavior can be observed, it is best to reduce the number of free parameters. We thus first nondimensionalized model 2:

$$\text{cytosolic SHR}: \quad \frac{dH'_c}{d\tau} = i - bS'H'_c + bdH'_n - H'_c \quad (5a)$$

$$\text{nuclear SHR}: \quad \frac{dH'_n}{d\tau} = H'_c S' - dH'_n - eH'_n \quad (5b)$$

$$\text{SCR}: \quad \frac{dS'}{d\tau} = \frac{fH_n'S'}{1+(H_n'+S')/g} + 1 - S'(w - R' - T') - vS' \tag{5c}$$

$$\text{CYCD6;1}: \quad \frac{dC'}{d\tau} = \frac{jH_n'S'}{1+(H_n'+S')/g} - kC' \tag{5d}$$

$$\text{RBR}^{\text{P}}: \quad \frac{dR'}{d\tau} = C'(w - R' - T') - mR' \tag{5e}$$

$$\text{SCR-RBR}: \quad \frac{dT'}{d\tau} = pS'(w - R' - T') - qT' \tag{5f}$$

Where $H_c' = \alpha H_c$, $H_n' = \beta H_n$, $S' = \beta S$, $C' = \delta C$, $R' = \varepsilon R$, $T' = \varepsilon T, \tau = \eta t$; the variable rescalings are given by $\alpha = c_{H_n}/(d_{H_c} z)$, $\beta = d_{H_c}/p_{S2}$, $\delta = c_R/d_{H_c}$, $\varepsilon = c_T/d_{h_c}$, and $\eta = d_{h_c}$; and the parameter rescalings are given by $i = p_{H_c} c_{H_n}/(z d_{H_c}^2)$, $b = c_{H_n} p_{S2}/d_{H_c}^2$, $d = c_{H_c}/d_{H_c}$, $e = d_{H_n}/d_{H_c}$, $f = p_{S1} p_{S2}/d_{H_c}^2$, $g = d_{H_c} c_S/p_{S2}$, $w = r c_T/d_{H_c}$, $v = d_S/d_{H_c}$, $j = p_C c_R p_{S2}^2 X^h/(d_{H_c}^4 (c_X^h + X^h))$, $k = d_C/d_{H_c}$, $m = d_R/d_{H_c}$, $p = c_T p_{S2}/d_{H_c}^2$, and $q = d_T/d_{H_c}$.

The previously derived QSS reduction of the model allowed us to very directly and rapidly verify for a broad range of different parameter settings if the model presents three equilibria and thus bistable behavior. To test whether the bistability is indeed a structural property of the model, we screened for the bistability while concurrently varying the values of all the nondimensionalized parameters given above. This analysis has been performed by randomly varying each parameter value over orders of magnitude around the default value (we present the results for 10-, 100-, 10000-, $10^6$- and $10^9$-fold variations). For the random value of each parameter we have used a log uniform distribution: $c = 10^{(\log_{10}(c_0) - \log_{10}(f)/2 + p(c,f))}$, where $c$ is the random value of the parameter; $c_0$ the default value of the parameter; $f$ the fold variation; and $p(c,f) = (H(c) - H(c - \log_{10}(f))/\log_{10}(f))$ the probability density function, in which $H$ is the Heaviside step function. For example, in the case of a 10,000-fold random variation around the value $c_0 = 1$, the values of parameter $c$ will lie between 0.01 and 100, and the probability of the parameter to be between 0.01 and 0.1 will be as large as the probability for it to lie between 0.1 and 1, between 1 and 10, or between 10 and 100. We first concurrently varied all parameters around default values that were calculated from the parameter values given in Table S2, using the parameter rescaling formulas shown above, for two different levels of auxin, $X = 1000$ and $X = 10{,}000$. The probability of bistability to appear in the system is shown in Table S3, based upon 10,000 random drawings for each fold-variation and default parameter setting. (Note, that due to the two feedback loops there also exists the possibility of having five equilibria, three of which being stable. This was typically observed in around 0.1% of the random drawings, and were counted to present the bistability as well.) We observe that the simplified model presents a very high level of robustness in behavior. For example, even with a billion-fold variation in all parameters, 26% of the simulations still present qualitatively similar behavior. There is also an "auxin" effect: For $X = 10{,}000$, the probability of finding bistability is lower when fold-variations are not as high as for $X = 1000$. This is due to the fact that for the default parameters at high levels of auxin the system is close to the bifurcation which can bring the cell to the ACD-related state. However, when a much larger parameter range is sampled, the probabilities to find bistability become much more comparable again, illustrating that the bistability is an overarching property of the model.

To check the importance of the specific choice of the default parameters in this analysis, we repeated the screening for bistability for the case where all the default values around which the parameters are varied in Equation 5 are set to unit value (one). Note that this could be considered the worst-case scenario, given that it corresponds to almost no influx of SHR ($i = 1$), very low total amounts of RBR that could bind to SCR ($w = 1$), and the amplification loops being almost always saturated ($g = 1$). But even for these very unfavorable parameter settings, adding sufficiently high levels of noise causes appearance of bistability in 5.8% of the cases. Even more striking, when we increased for those three parameters their default value to 1,000, while keeping all other parameters at a value of 1, the incidence rate of bistability turned out to be even higher than around the parameter values as used throughout the rest of the paper. We therefore conclude that one of the key behaviors of the model is presenting bistability over a wide parameter range.

Finally we checked if robustness of the bistable switch indeed corresponds to robustness of the spatial patterning, by determining the range over which qualitatively the same pattern (i.e., only QC and CEI/CEID presenting the ACD cell state) can be observed in spatial simulations when each parameter value is varied individually while keeping all others at their default value (see the last column in Table S2). To perform the simulations within reasonable computational time, simulations were started at the final configuration of the previous parameter setting, as it was unfeasible to do massive screenings of fully randomized parameters. These simulations revealed that for all parameters the range over which the correct patterning can be observed is again very large.

In short, model 2, or the "auxin-regulated double positive-feedback model" (1) has the *minimal requirements* to confine the ACD behavior to a single cell at a specific location; (2) shows that the molecular network integrates an interplay between the radial SHR gradient and the longitudinal auxin gradient; (3) shows that the switching behavior is very general and robust, causing the right cells to enter the ACD cell state over a wide parameter range.

*Spatial Simulations of Model 2 Show that, Unlike Model 1, SHR Does Not Remain Confined to the Endodermis.* While, compared to model 1, model 2 clearly presents an improvement in capturing the regulation of the ACDs, it nevertheless fails to explain the confinement of SHR to the endodermis. This is because in model 2 only the cells which enter the ACD state can block the SHR throughput from the vasculature to the external cell files. It therefore allows SHR to move from the endodermal cells into the cortex, because those endodermal cells are not in the ACD state. Not only this is unlike what is observed experimentally, but it also reduces the robustness of the dynamics regarding the radial aspect of the patterning.

### Model 3 or "Full Model": SHR Confinement

In model 2, SHR ends up in the cortex and epidermis, because RBR binding to SCR suppresses the interaction of SCR with SHR, thereby preventing the nuclear localization of SHR. The experimental observation that SHR remains confined to the endodermis suggested to us that this assumption was incorrect and that RBR binding to SCR does not prevent SCR to interact with SHR. This was further strengthened by the observation that *src* mutants do not present such a nuclear localization of SHR in the endodermis. So it rather seemed to be the case that RBR prevents SHR-SCR to activate downstream targets. In short, the modeling suggested that a ternary complex of SHR-SCR-RBR can be formed, for which we were later able to gather experimental evidence. We therefore extended model 2 to explicitly take into account not only the SCR-RBR complex, but also the SHR-SCR and SHR-SCR-RBR ternary complex.

Figure 5A shows the regulatory network of model 3. While in the previous models the combined action of SCR and nuclear SHR was introduced without this combined action necessarily having to be based on complex formation, we here take an explicit formation of a SHR-SCR complex into account (compare Figure 5A to Figure 4L). SCR continues to influence the nuclear localization of SHR, but now by explicitly forming a complex that is located in the nucleus, instead of promoting the entry rate of SHR from the cytosol into the nucleus. The equations are as follows:

$$\text{SHR}: \quad \frac{dH}{dt} = p_H - c_A SH - c_{U2} TH - d_H H \tag{6a}$$

$$\text{SCR}: \quad \frac{dS}{dt} = p_{S1} A + p_{S2} - c_A SH - c_T S(r - R - T - zU) - d_S S \tag{6b}$$

$$\text{SHR-SCR}: \quad \frac{dA}{dt} = \frac{c_A SH}{z} - d_A A - c_U A(r - R - T - zU) \tag{6c}$$

$$\text{CYCD6;1}: \quad \frac{dC}{dt} = p_C \frac{X^h}{c_X^h + X^h} A - d_C C \tag{6d}$$

$$\text{RBR}^{\text{P}}: \quad \frac{dR}{dt} = c_R C(r - R - T - zU) - d_R R \tag{6e}$$

$$\text{SCR-RBR}: \quad \frac{dT}{dt} = c_T S(r - R - T - zU) - d_T T - c_{U2} TH + d_U zU \tag{6f}$$

$$\text{SHR-SCR-RBR}: \quad \frac{dU}{dt} = c_U A(r - R - T - zU) + \frac{c_{U2} TH}{z} - d_U U \tag{6g}$$

Cytosolic, unbound SHR, $H$, has a basic production rate ($p_H$) and can bind to either SCR, $S$ ($c_A SH$), or to the SCR-RBR complex, $T$ ($c_{U2} TH$). This leads to the formation of the SHR-SCR complex, $A$, and the SHR-SCR-RBR ternary complex, $U$, respectively. Again we describe all complex formations as irreversible processes, to prevent the addition of many more parameters that have not yet been experimentally established, but we have assured ourselves that the temporal and spatial dynamics do not change when we take all the different possibilities of the complexes dissociating into account as well, as long as the kinetic rates are sufficiently balanced toward association (data not shown). All variables have again a basic turnover/decay (given by $d_H H$, $d_A A$, $d_S S$, $d_C C$, $d_R R$, $d_T T$, and $d_U U$). The $d_S$ term captures the SCR degradation, considered to be as large as $d_T$, the degradation of SCR-RBR. The parameter $d_R$ is capturing both degradation and dephosphorylation of $\text{RBR}^{\text{P}}$. Regarding the turnover/decay terms, we made the following three choices. First, given that large fluctuations in total RBR have not been experimentally observed, we opted for describing RBR as a constant pool (the regulation of which is kept out of the scope of this paper) in order not to further expand the number of variables in the model, preventing introduction of more parameters that would capture processes currently unclear and irrelevant for the dynamics of and insights from the model study. Specifically, we wanted to leave open whether loss of phosphorylated RBR occurs due to degradation or dephosphorylation currently unknown. By capturing RBR as a constant pool, both scenarios lead to exactly the same equations within the framework presented here. Second, we explicitly assume the complex dissociation sequence

SHR-SCR-RBR → SCR-RBR → RBR, again to limit the number of terms in the model and the associated parameter space. Thus, $d_U$ describes the transition from SHR-SCR-RBR to SCR-RBR, due to the degradation of SHR, considered to be as large as $d_H$. Third, following our policy of leaving out all the dissociation terms forced us into having to make one non-trivial decision. Decay of SCR when it is bound within the ternary SHR-SCR-RBR complex implies dissociation of SHR and RBR. Hence, if we would include this decay, we would introduce one dissociation term into the model, which we felt to be confusing. Alternatively, we could simply leave out this decay term. We opted for the latter, given that it prevents the addition of yet three more terms to the model and only marginally influences the dynamics, as we have tested in a version which includes every single dissociation term.

There is again a small background production of SCR, $S$ $(p_{S2})$, but its production can be geared up by the SHR-SCR complex, $A$ $(p_{S1}A)$. Because we now explicitly describe the formation of the complex underlying downstream activation, there is no need anymore to introduce a saturation in those terms. SCR can bind to RBR, to form SCR-RBR, $T$. Assuming that the total amount of RBR per cell remains constant (given by the parameter $r$), but that only the non-phosphorylated form can bind to SCR, the total amount of RBR that is available to bind is given by total RBR, minus the amount of $RBR^P$, $R$, as well as all RBR already in a complex (i.e., SCR-RBR, $T$, and SHR-SCR-RBR, $U$). Taking this into account, the total amount of RBR available to bind equals $(r - R - T - U)$, and the rate by which SCR binds to RBR is therefore given by $c_T S(r - R - T - U)$. Regarding the SHR-SCR complex, $A$, we take the view that although SCR is already bound to SHR, it can still bind to RBR as well, to form the SHR-SCR-RBR ternary complex, $U$ $(c_U A(r - R - T - U))$. The combined action of the SHR-SCR complex, $A$ (but not the SHR-SCR-RBR ternary complex, $U$) is able to activate the production of CYCD6;1, $C$ $(pcX_h/(c_X^h + X^h)A)$. Finally, CYCD6;1, in its turn, causes phosphorylation of non-phosphorylated RBR $(c_R C(r - R - T - U))$. Note that this equation for $RBR^P$ implicitly assumes that de novo RBR production gives rise to non-phosphorylated RBR only, while CYCD6;1 is essentially required for its phosphorylation.

Because both the SHR-SCR complex, $A$, and the ternary complex, $U$, are nuclearly localized, the correction term $z$ is also required for the formation of the ternary complex from SHR and SCR-RBR. For the binding of RBR to SHR-SCR no such correction factor is needed because both SHR-SCR and the ternary complex are nuclearly localized. Also in the calculation of the total amount of RBR that is available to bind, it has to be taken into account that the ternary complex is only nuclearly localized and therefore presents a smaller contribution to the reduction of available RBR. Hence, the total amount of RBR available to bind now equals $(r - R - T - zU)$. Moreover, to capture the degradation SHR-SCR-RBR → SCR-RBR, which implies a nuclear to cellular transition, the correction factor $z$ is also required. Moreover, we assumed that binding of SHR to SCR does not depend on whether SCR is already bound to RBR $(c_A = c_{U2})$, and likewise, that binding of RBR to SCR does not depend on whether SCR is already bound to SHR $(c_T = c_U)$.

A strict parameter mapping from model 2 to model 3 is missing, given that we introduced the SHR-SCR complex and the SHR-SCR-RBR ternary complex. Nevertheless, most parameters have the same meaning and units as in model 2, and we therefore mainly used the same values, to ensure that the comparison between the models is biologically meaningful. Moreover, we took the reasonable choices that $c_A = c_{H_n}$ and $d_A = d_{H_n}$. However, the parameters $p_C$ and $p_{S1}$ changed units, due to the fact that the previous model did not describe the SHR-SCR complex explicitly, hence for those parameters a direct mapping was not possible. To enable model comparisons in a fair manner, the parameters $p_C$ and $p_{S1}$, as well as the value of $p_{S2}$, were chosen, such that the bifurcation points in model 1 and 2, as shown in Figures 3H and 4M, and in model 3, as shown in Figures S4N and S4O, are positioned at comparable values, within a 25% variation range. For the same reason we also modified the value of $c_R$. (Note that we did not fine-tune the parameters to carefully match the bifurcation points.) Finally, to obtain comparable spatial patterns, we also modified the value of $p_H$, compared to the value of $p_{H_c}$ used previously.

*The Importance of the Ternary Complex: SHR Confinement.* Model 3 again presents two clearly distinct cell states, with only the QC and CEI/CEID cells entering the ACD cell state. The third model presents in a parsimonious way our current understanding of the regulatory circuit underlying ACDs. It is, however, too intricate to allow for nullcline analysis, as presented in Figures 3I–3L and S2E–S2H, or large-scale parameter screening, as presented in Table S3. Nevertheless, we assured ourselves that when the further extensions were included, the model still presented robust radial and lateral specification of the ACD cell state. We did so by first determining again, through bifurcation analysis, for each individual parameter the range over which bistability can be observed when that parameter is varied while keeping all others at their default values. The ranges are given in the one but last column in Table S4. Next, we determined again, through spatial computer simulations, the parameter range for which we do not observe any perturbation in the spatial pattern, once this is established for the default parameter setting (i.e., when starting with the pattern as shown in Figures 5C–5G and S4I–S4M). The obtained parameter ranges are given in the last column of Table S4. Together, it shows that both the bistability and the spatial pattern formation are again a robust feature of the model. Moreover, the model presents SHR confinement in the endodermis, without flipping to the ACD cell state, through the formation of the ternary complex. The robustness of the spatial patterning in the radial direction is caused by the "capturing" the SHR in the endodermal layer, which prevents other cell files to gain the potential to reach high SHR-SCR levels. The robustness in the transversal direction is due to the fact that the switch to the ACD state requires sufficiently high auxin levels, right in the region where the auxin gradient is steepest.

In short, model 3, or the "full model" (1) can explain both ACD localization and SHR restriction and (2) is highly robust.

### *Reset: Turning Off the ACD-Related Cell State during Asymmetric Cell Division*

Until now we have been showing that the bistability is advantageous for conferring precision and robustness, but concurrently it presents the problem of how to turn the ACD-state off during tissue dynamics. We therefore finalize by explaining the importance of a "reset" during cell division, how the reset-mechanism functions within model 3, for which we again have gained experimental

evidence. While high auxin levels are able to sufficiently augment the CYCD6;1 feedback loop to bring the CEI cell into the ACD-related or "on" state, it is not inversely true that a low auxin level can bring the cell back into the "off" state (Figures 4M and 7F). We explored whether increased protein degradation during the cell cycle progression could cause the cell to switch off. To do so, we studied in the third, full model the effect of increased protein degradation, taking two possible scenarios into account. The first possibility that we explored is an equally increasing breakdown of SHR, SCR, RBR and all the complexes that they form. Such a scenario can be captured by multiplying all decay terms in Equation (6) with a factor $d$ which describes the increased protein degradation level (i.e., $d_H$ becomes $d \times d_H$, $d_S$ becomes $d \times d_S$, etc, for all $d_H$, $d_S$, $d_A$, $d_C$, $d_R$, $d_T$, $d_U$). When $d = 1$, we capture the default situation, while $d>1$ describes increased protein degradation levels (and $d<1$ reduced degradation levels). The second scenario is that increased protein degradation does not act on complexes, but is restricted to the free proteins. In this scenario, the factor $d$ would only affect $d_H$, $d_S$, $d_C$, and $d_R$.

Now to test whether this could "reset" the CEID, we analyzed the dynamics of that cell within the full ODE model, using, by probing the spatial model at steady state, its correct auxin level ($X$ = 5223 a.u.); SHR influx ($p_H$ = 332.5a.u./h); and relative size of the nucleus ($z$ = 0.07634). Figure 6L shows a bifurcation diagram for the equilibrium level of SHR-SCR, $A$, as a function of the increased level of protein degradation for the first scenario, in which all protein degradation can become elevated. It can be seen that when $d = 1$, i.e., when there is no elevated protein degradation, there are three equilibria, two of which are stable. This implies that the neighboring shootward cell of the CEI within the endodermal cell file could indeed be either in the "on" state or in the "off" state, but having inherited its state from the CEI would be expected to be in the "on" state. If, however, the ACD takes place concurrently with increased protein degradation, the picture becomes different: when $d > 2.426$, the "on" equilibrium disappears through a fold bifurcation, and the dynamics are expected to move to the "off" equilibrium. In short, a 2.5 times higher protein degradation rate is sufficient to cause the system to switch off.

Figure S5X presents the second scenario, in which complexes are not available for accelerated degradation. Even though in this scenario the complexes themselves do not undergo increased breakdown, again the "on" equilibrium disappears at higher degradation levels, but now requiring values of $d > 5.401$, more than twice as high as in the first scenario. Thus, the rapid breakdown of their substrates can cause a sufficient reduction in complex formation to bring the cell into the "off" state. We do not modify in these simulations the total amount of RBR, which effectively implies a higher turnover during this phase of the cell cycle.

A phase of accelerated protein degradation during the cell cycle will inevitably be of a limited duration. While in Figures 6L and S5Y we focused on the disappearance of the "on" state, this does not automatically guarantee that the cell will end up in the "off" state. When the time span of the accelerated protein degradation is too short, the dynamics could relapse if during this phase it has not passed the separatrix formed by the stable manifold of the saddle point which separates the basins of attraction of the two stable equilibria. Figure S5Z shows the time dynamics for both a too short (15 min, dashed lines) and sufficiently long (1 hr 30 min, continuous lines) time span of accelerated protein degradation ($d$ = 10), after which protein degradation returns to the default level ($d$ = 1), depicted for both scenarios. The dynamics starts from the "on" state when, at time = 0 hr accelerated protein degradation is initiated. If the time span is too short, a relapse to the "on" state can be observed, while a sufficiently long time span causes the dynamics to settle in the "off" state. Note that in the first scenario the initial drop is faster, and hence the time span required is shorter. Also note the undershoot that can be observed for the second scenario. This is due to the fact that increased nondiscriminatory protein degradation has not only a negative, but also a positive effect on SHR-SCR levels because increased complex breakdown reduces buffering through the ternary complex. In the second scenario, however, this positive effect is lacking.

The importance of the right balance between the level of accelerated protein degradation and the time interval during which accelerated degradation takes place, is further illustrated in Figure 6M, for the first scenario. It shows that for a four-fold increase in protein degradation a time window of 40 min is not sufficient for turning the cell "off"', while a 10-fold increase in protein degradation turns the cell off, even when the time window is as short as 40 min. If the timescale were instead two hours, also a four-fold increase in protein degradation suffices to change the cell state. Also note that the fast degradation rates can trigger transient oscillatory dynamics.

***Specific Extra Details Regarding the Simulations Presented in Figures 3, 4, 5, 6, S2, S4, and S5***

In the simulations of model 1, we used $p_C = 1$ for Figures 3N, 3P, and 3R, $p_C = 50$ for Figures 3O, 3Q, and 3S, and $p_C = 0$ a.u.$^{-1}$h$^{-1}$ for Figure 3H. All other parameter values used are as given in Table S2. The relative nucleus size $z$ and auxin concentration $X$ used for the ODE analyses are based upon the size of the CEI in the spatial simulations ($z$ = 0.0185787) and its equilibrium auxin level ($X$ = 16054.8 a.u.). While $p_{H_c}$ (model 1 and 2) and $p_H$ (model 3) in the spatial models describe the SHR production in the vasculature, we instead used in the ODE analyses the effective SHR influx into the CEI, as measured at equilibrium ($p_{H_c} = p_H = 137.5$ a.u. h$^{-1}$). (Note that in the spatial simulations those values vary in both space and time.) In Tables S2 and S4, both the value used in the spatial simulations and the value used in the ODE analyses are given. Moreover, in Figure S4N we have indicated typical SHR influx into CEI and cortex (137.5 and 13.1 a.u. h$^{-1}$, respectively). For the bifurcation diagrams and time series regarding the resetting (Figures 6L, 6M, S5Y, and S5Z), we focused on the first endodermal cell, which due to the increased protein turnover should be prevented to undergo another ACD. Again, we used the values as observed in the spatial simulations: ($z$ = 0.07634; $X$ = 5223 a.u.; $p_{H_c} = p_H = 332.5$ a.u. h$^{-1}$.

To describe the SCR$^{AxCxA}$ mutant in Figures 5I–5L, we reduced the binding rate between SCR and RBR by 75% ($c_T = c_U = 0.1$). To describe the auxin treatment in Figures 5K and 5L, we immersed the root in a medium with auxin, creating an extra influx of auxin along the whole edge of the root of 5 a.u./$\mu$m.

Auxin is calculated at a subcellular resolution, which can be noticed in Figure 4N. All other variables are calculated at a cellular resolution. We indicate the observed levels by color-coding each cell to represent its cellular concentration. The auxin (*X*), CYCD6;1 (*C*), and nuclear SHR ($H_n$) or SHR-SCR (*A*) concentration are displayed on a logarithmic scale, while (cytosolic) SHR ($H_c$, *H*) and SHR-SCR-RBR (*U*) are displayed on a linear scale. Moreover, for SHR-SCR-RBR (*U*), the color-coding is proportional to the total amount per cell rather than its concentration (i.e., plotted is $U \cdot z$), which is more meaningful. For straightforward comparison between the different treatments, the same color scale is used for both the wild-type and the mutants. This was done by fixing the minimum and maximum values for each of the displayed outputs to the values in the wild-type simulations that include auxin, except for SHR-SCR-RBR (*U*), where we fixed it to 20% of total RBR ($0.2 \cdot r$). Consequently, for the mutants and treatments the visual representation of the differences was truncated for values that were higher than the highest value in the wild-type or lower than the lowest value in the wild-type. Specifically, the minimum and maximum values in the color encoding were fixed to (in a.u.) *X*: $[34.5, 4.54 \times 10^4]$; $H_c$: [0,647]; *H*: [0,42]; $H_n$: $[10^{-4}, 10^6]$; *A*: $[10^{-4}, 10^4]$; *C*: $[10^{-3}, 5 \times 10^7]$; *S* (model 1,2): $[10^2, 10^8]$; *S* (model 3): $[10^{-4}, 10^6]$.

## SUPPLEMENTAL REFERENCES


Boisnard-Lorig, C., Colon-Carmona, A., Bauch, M., Hodge, S., Doerner, P., Bancharel, E., Dumas, C., Haseloff, J., and Berger, F. (2001). Dynamic analyses of the expression of the HISTONE:YFP fusion protein in *arabidopsis* show that syncytial endosperm is divided in mitotic domains. Plant Cell *13*, 495–509.

Borghans, J.A.M., de Boer, R.J., and Segel, L.A. (1996). Extending the quasi-steady state approximation by changing variables. Bull. Math. Biol. *58*, 43–63.

Cutler, S.R., Ehrhardt, D.W., Griffitts, J.S., and Somerville, C.R. (2000). Random GFP:cDNA fusions enable visualization of subcellular structures in cells of *Arabidopsis* at a high frequency. Proc. Natl. Acad. Sci. USA *97*, 3718–3723.

Friml, J., Vieten, A., Sauer, M., Weijers, D., Schwarz, H., Hamann, T., Offringa, R., and Jürgens, G. (2003). Efflux-dependent auxin gradients establish the apical-basal axis of *Arabidopsis*. Nature *426*, 147–153.

Heisler, M.G., Ohno, C., Das, P., Sieber, P., Reddy, G.V., Long, J.A., and Meyerowitz, E.M. (2005). Patterns of auxin transport and gene expression during primordium development revealed by live imaging of the *Arabidopsis* inflorescence meristem. Curr. Biol. *15*, 1899–1911.

Jaeger, J., Irons, D., and Monk, N. (2008). Regulative feedback in pattern formation: towards a general relativistic theory of positional information. Development *135*, 3175–3183.

Nakajima, K., Sena, G., Nawy, T., and Benfey, P.N. (2001). Intercellular movement of the putative transcription factor SHR in root patterning. Nature *413*, 307–311.

Weingartner, M., Criqui, M.-C., Mészáros, T., Binarova, P., Schmit, A.-C., Helfer, A., Derevier, A., Erhardt, M., Bögre, L., and Genschik, P. (2004). Expression of a nondegradable cyclin B1 affects plant development and leads to endomitosis by inhibiting the formation of a phragmoplast. Plant Cell *16*, 643–657.

Xie, Z., Lee, E., Lucas, J.R., Morohashi, K., Li, D., Murray, J.A.H., Sack, F.D., and Grotewold, E. (2010). Regulation of cell proliferation in the stomatal lineage by the *Arabidopsis* MYB FOUR LIPS via direct targeting of core cell cycle genes. Plant Cell *22*, 2306–2321.

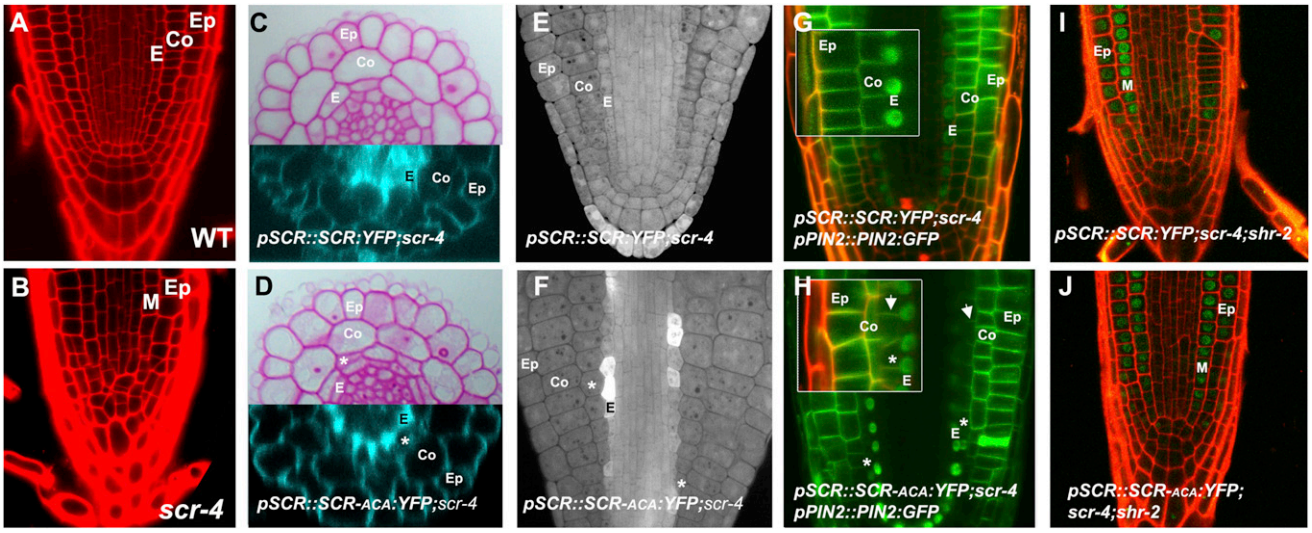


**Figure S1. RBR-SCR Interaction Inhibits Asymmetric Cell Division in the Ground Tissue, Related to Figure 1**

(A–J) Confocal laser scanning microscope (CLSM) of WT (A) and scr-4 (B) roots. CLSM and Nomarski optics of longitudinal and transverse root sections of 5 dpg. *scr4-1* plants complemented with WT SCR (C, E, and G) or with $SCR^{AxCxA}$ (D, F, and H). Combined Nomarski and confocal images of transverse section showing cell file composition (top) and casparian strip (bottom) in WT root (C) and $SCR^{AxCxA}$ root (D) (transverse root sections; extra cell layer does not contain casparian strip). Aniline blue staining of mature embryo shows extra layer in $SCR^{AxCxA}$ (E–F, asterisk). CLSM of *pPIN2::PIN2:GFP* introgressed in *scr4-1*/SCR WT (G) and in *scr4-1*/$SCR^{AxCxA}$ (H); insets highlight differences in ground tissue layers and localization of PIN2-GFP protein fusion. Arrow heads in (H) point to polar PIN2 localization in the extra cell layer. CLSM images of *scr4-1;shr2* double mutant transformed with the SCR and $SCR^{AxCxA}$, respectively (I and J). In all panels, Ep: Epidermis, Co: Cortex, E: Endodermis, Asterisk: extra layer.

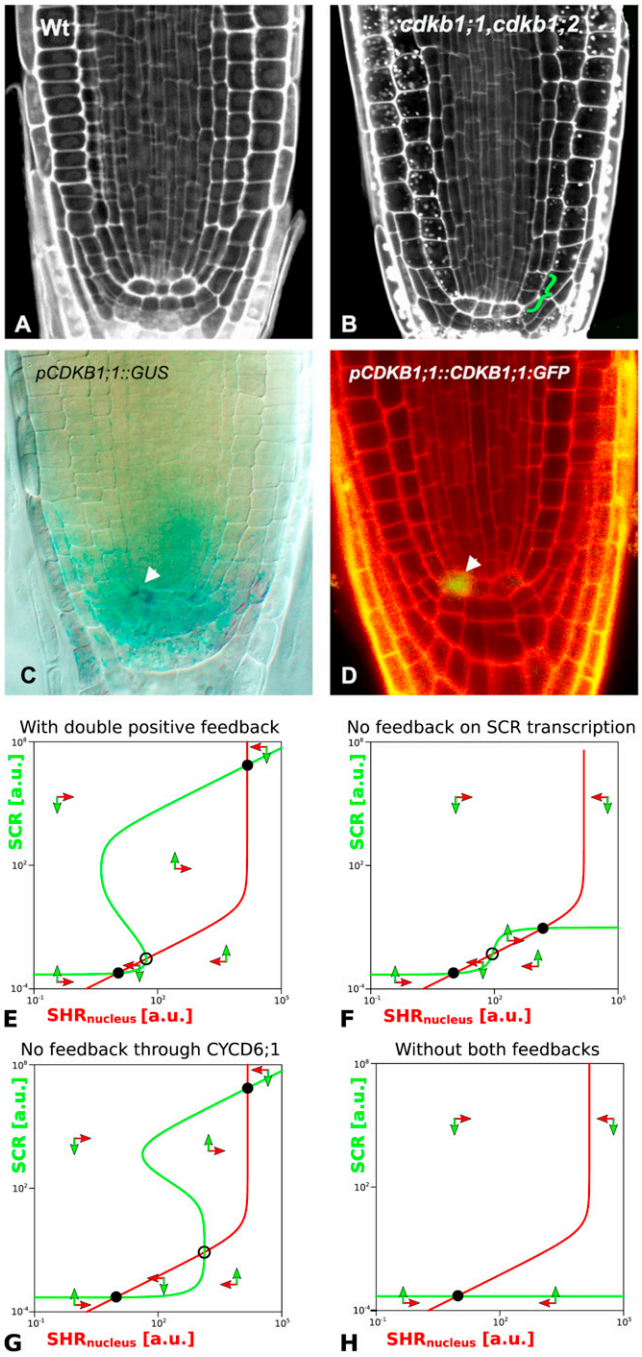


**Figure S2. Involvement of *CDKB1;1* and *CDKB1;2* in ACDs and Untangling of Feedback Loops, Related to Figure 3**

(A–D) *CDKB1;1* is specifically expressed in the ground tissue initials and, in redundancy with *CDKB1;2*, modulates ACDs. Phenotype of WT (A) and *cdkb1;1 cdkb1;2* double mutant (B) roots of 4 dpg seedlings showing a delay in periclinal division of the CEID in the later (bracket). Expression patterns of the transcriptional fusion *pCDKB1;1::GUS* (C) and the translational fusion *pCDKB1;1::CDKB1;1:GFP* (D) revealing the high specific domain CDKB1;1 in the ground tissue initials (arrowheads).

(E–H) Bistability and feedback loops. Phase-plane analysis and nullclines of model 1 under QSS conditions. (E) Model 1 presents two stable equilibria (solid black circles; one of high SCR and nuclear SHR levels, the other of low SCR and nuclear SHR levels), separated by an unstable equilibrium (open circle, saddle point). (F) When the activation mediated by CYCD6;1 is turned off, the model continues presenting similar equilibrium points and overall dynamics. (G) When the feedback of SCR and nuclear SHR on *SCR* transcription is not taken into account, the model still presents the characteristic bistability, although the high equilibrium and low equilibrium are now quantitatively less distinct. (H) Without either of these feedbacks, the system fails to produce bistability. Only one steady state is possible for any parameter setting, in which free SCR (unbound to RBR) and nuclear SHR remain low.

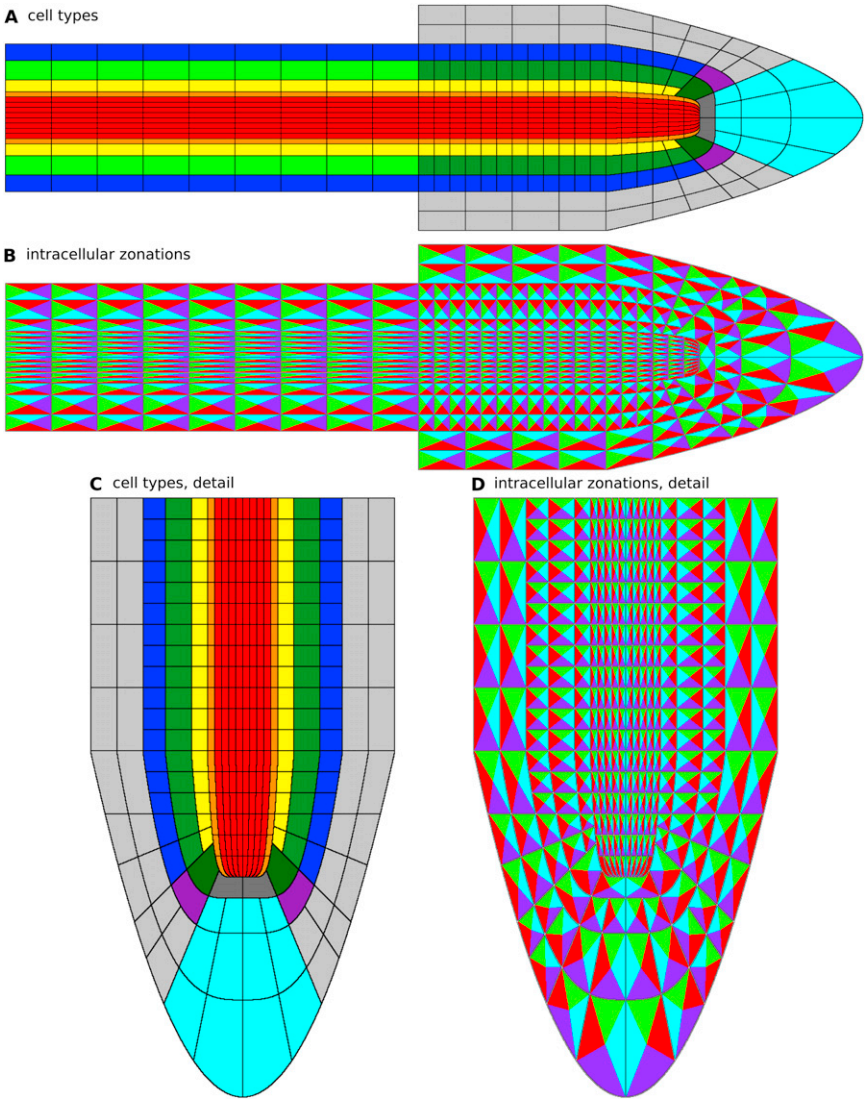


**Figure S3. Layout of the Root and Orientation of the Individual Cells, Related to Figure 4**

(A) The different cell types within the caricature root layout. Color coding to indicate the cell types is shown in Table S1.

(B) Zonations indicating the upward (green), downward (purple), inward (cyan), and outward (red) part of the cell, used to correctly position within the model the PIN proteins, as indicated in Table S1.

(C and D) Enlargement of (A and B) in the Meristem Zone.

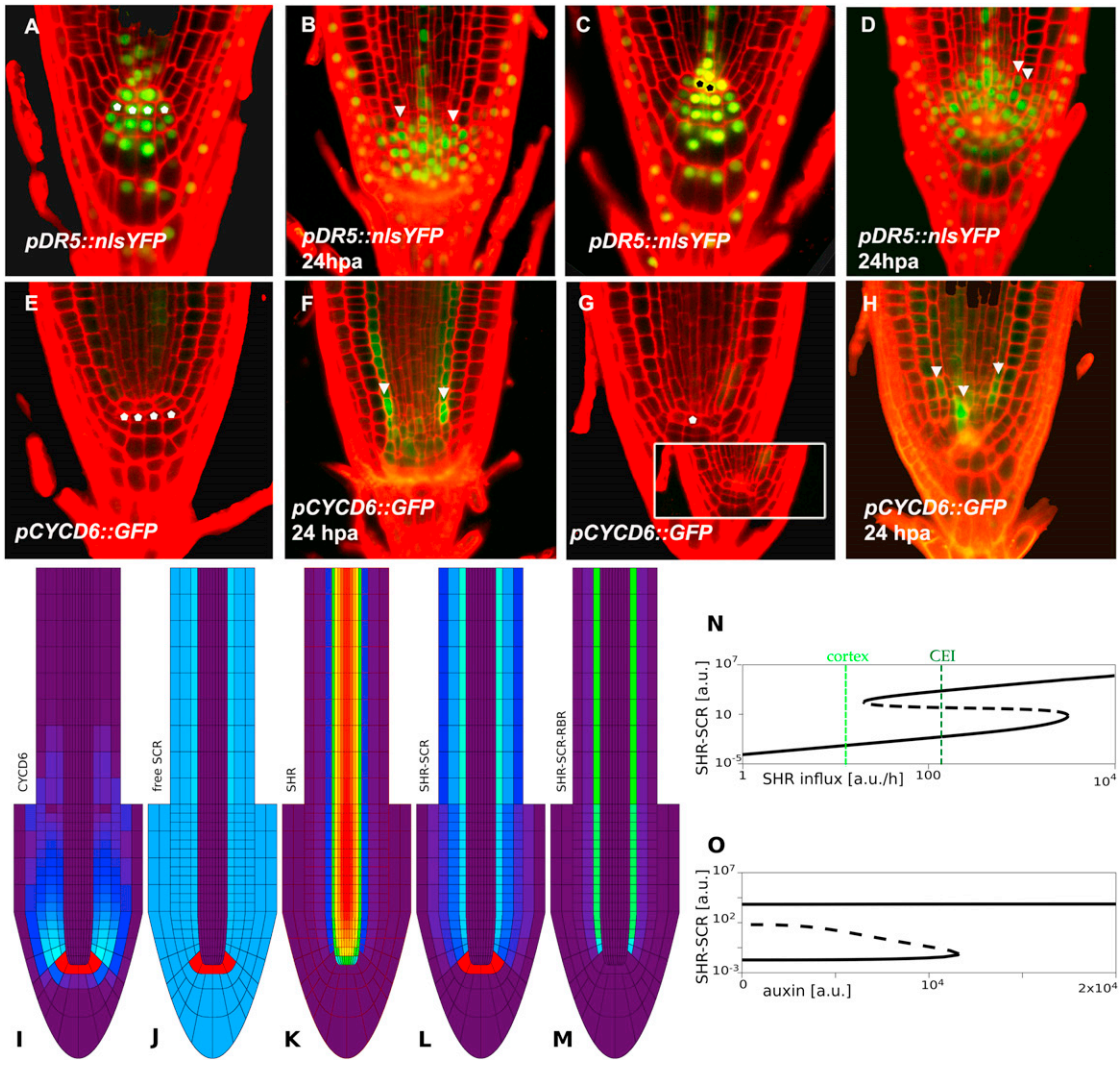


**Figure S4. Auxin Concentration Influences *CYCD6;1* Expression, Producing a Bias toward the Stem Cell Region for the Ground Tissue ACDs; SHR Confinement in Model 3, Related to Figure 5**

(A–H) Laser ablation-induced auxin redistribution alters *CYCD6;1* expression. Expression patterns of *pDR5::nlsYFP* in roots before (A) and after (B) columella stem cell ablations, as well as before (C) and after (D) QC ablation. Expression patterns of *pCYCD6;1::GFP* in roots before (E) and after (F) columella stem cell ablation, and before (G) and after (H) QC ablation. Inset in G highlights the specific death of the QC cells 2 hr after the ablation. White and black pentagons show the chosen cell for ablation. White arrowheads point to the change in expression for both markers mainly in the endodermis, cortex and vascular tissues.

(I–O) Model 3 presents both bistable switch and SHR confinement. (I–M) Complete expression profiles of the simulation presented in Figures 5C–5G. (I) CYCD6;1 (*C*); (J) free SCR (*S*); (K) SHR (*H*); (L) SHR-SCR (*A*); and (M) SHR-SCR-RBR (*U*) levels. (See also Movie S1.) (N) Bifurcation diagram showing the equilibrium SHR-SCR complex level (*A*) as a function of SHR influx ($p_H$) The dashed line indicates an unstable equilibrium. (O) Bifurcation diagram showing the equilibrium SHR-SCR level as a function of the auxin level (*X*).

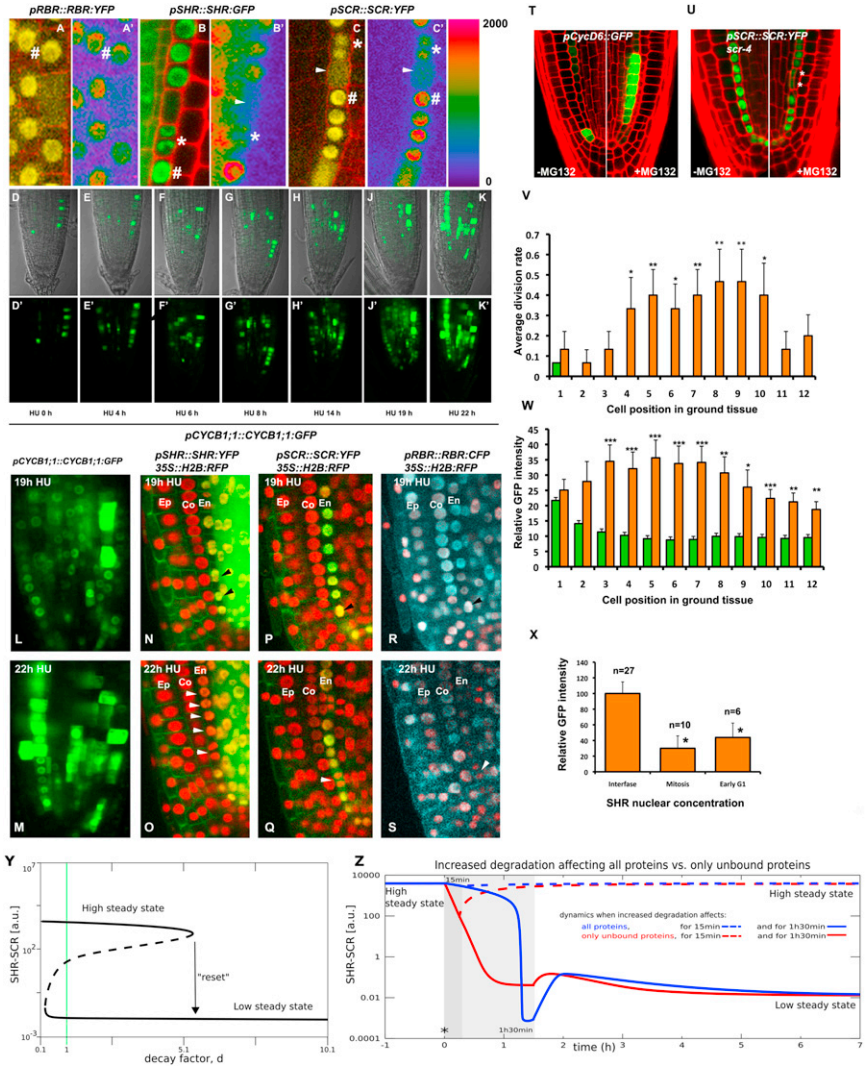


**Figure S5. Experiments and Modeling on Protein Degradation of SCR, RBR, and SHR and Synchronization Test in Roots, Related to Figure 6**

(A–S) Protein localization and intensity of pRBR::RBR:YFP (A) and corresponding heat map (A′), pSHR::SHR:GFP (B) and corresponding heat map (B′), pSCR::SCR:YFP (C) and corresponding heat map (C′); during different cell stages, i.e., prior division (#), during division (arrowhead) and in daughters (asterisk). Heatmap units refer to fluorescence intensity given as average pixels/area. In order to associate in detail protein degradation with cell cycle stage (as described in detail in Figure 6) first we established a time course for cell cycle synchronization induced with HU, revealed by the expression dynamics of pCYCB1;1:: CYCB1;1:GFP in roots meristems at 0 hr (D and D′), 4 hr (E and E′), 6 hr (F and F′), 8 hr (G and G′), 14 hr (H and H′), 19 hr (J and J′) and 22 hr (K and K′) after transference to HU. CLSM im- ages after 19 hr of treatment with Hydroxyurea (19 hr HU) (L, N, P, and R) and at 22 hr HU (M, O, Q, and S). pCYCB1;1:: CYCB1;1:GFP (L and M); pSHR::SHR:YFP/p35S::H2B:RFP (N and O); pSCR::SCR:YFP/p35S::H2B:RFP (P and Q); and pRBR::RBR:CFP/p35S::H2B:RFP (R and S). Black arrowheads point to cells prior to mitosis, white arrowheads denote the same cells during or after mitosis.

(T and U) (T) *pCycD6::GFP* or (U) *pSCR::SCR:YFP* plants were treated with mock or 50 μM MG132 for 20 hr and analyzed by CLSM.

(V) Extra periclinal cell divisions in the endodermis were quantified for each position in the endodermis; CEI = position 1, n = 15.

(W) Quantification of fluorescence of CycD6-GFP plants treated with mock or 50 μM MG132 for 20 hr and normalized against CEI average for each position in the endodermis; CEI = position 1, n = 15. Significance in V, W was analyzed by t test: * $0.01 < p < 0.05$; ** $0.001 < p < 0.0001$; ***$p < 0.0001$.

(X) Quantification of fluorescence of SHR-GFP during and after mitosis within the nuclei or condensed chromosomes. Asterisks mark $p < 0.05$.

(Y) Bifurcation diagram showing equilibrium SHR-SCR levels for Equation (6) as a function of the level of enhanced protein degradation in the case the enhancement only affects unbound protein. To capture environment of CEID/first endodermal cell, $X$ = 5223 a.u.; $p_H$ = 332.5 a.u./h; $z$ = 0.07634, all other parameters are as in Table S4.

(Z) Time dynamics for short (15 min, dashed lines) and long (1 hr 30 min, continuous lines) time span of accelerated protein degradation ($d$ = 10), after which protein degradation returns to the default level ($d$ = 1). Red lines depict dynamics for enhanced degradation of all proteins, blue lines for enhanced degradation of unbound proteins.